Article

Wide-temperature-range thermoelectric n-type $Mg_3(Sb,Bi)_2$ with high average and peak zT values

Jing-Wei Li[1], Zhijia Han[2], Jincheng Yu [1], Hua-Lu Zhuang [1] ✉, Haihua Hu[1], Bin Su [1], Hezhang Li[1], Yilin Jiang [1], Lu Chen[1], Weishu Liu [2], Qiang Zheng [3] & Jing-Feng Li [1] ✉

$Mg_3(Sb,Bi)_2$ is a promising thermoelectric material suited for electronic cooling, but there is still room to optimize its low-temperature performance. This work realizes >200% enhancement in room-temperature zT by incorporating metallic inclusions (Nb or Ta) into the $Mg_3(Sb,Bi)_2$-based matrix. The electrical conductivity is boosted in the range of 300–450 K, whereas the corresponding Seebeck coefficients remain unchanged, leading to an exceptionally high room-temperature power factor >30 $\mu W\ cm^{-1}\ K^{-2}$; such an unusual effect originates mainly from the modified interfacial barriers. The reduced interfacial barriers are conducive to carrier transport at low and high temperatures. Furthermore, benefiting from the reduced lattice thermal conductivity, a record-high average zT > 1.5 and a maximum zT of 2.04 at 798 K are achieved, resulting in a high thermoelectric conversion efficiency of 15%. This work demonstrates an efficient nanocomposite strategy to enhance the wide-temperature-range thermoelectric performance of n-type $Mg_3(Sb,Bi)_2$, broadening their potential for practical applications.

Thermoelectric (TE) technology that enables the direct conversion between heat and electricity is a promising approach to easing the fossil fuel shortage and promoting the sustainable development[1,2]. The energy conversion efficiency of TE devices is determined by the performance of TE materials, which is characterized by the dimensionless figure of merit, $zT = S^2\sigma T/(\kappa_L + \kappa_e)$, where S is the Seebeck coefficient, σ is the electrical conductivity, T is the absolute temperature, κ_L is the lattice thermal conductivity, and κ_e is the electronic thermal conductivity. Considering that S, σ, and κ_e are strongly coupled with each other through the carrier concentration, the key to enhancing the TE performance lies in decoupling or synergistically controlling these TE parameters.

Most TE materials, such as $PbTe$[3,4], $SnSe$[5,6], and Cu_2Se[7,8], exhibit superior performance at high temperatures (approximately above 773 K), whereas their room-temperature performance is inferior to the commercial Bi_2Te_3[9,10]. However, due to the high cost of Te element, it is vital to seek and develop economical substitutes for Bi_2Te_3 to further scale up TE device fabrication[11,12]. Currently, $Mg_3(Sb,Bi)_2$ is rendered as an ideal candidate for near-room-temperature applications, owing to the superb TE performance at low temperatures originating mainly from the intrinsically low κ_L as a result of its complex crystal structure[13–16]. Meanwhile, the multivalley characteristics of n-type $Mg_3(Sb,Bi)_2$ can ensure outstanding electrical transport properties, beneficial to yielding high TE performance.

In recent years, the near-room-temperature performance of $Mg_3(Sb,Bi)_2$ has been improved by multiple strategies. By constructing the solid solutions with different Bi to Sb ratios, the band structure could be modified and the peak zT value shifted towards a lower

[1]State Key Laboratory of New Ceramics and Fine Processing, School of Materials Science and Engineering, Tsinghua University, Beijing 100084, China. [2]Department of Materials Science and Engineering, Southern University of Science and Technology, Shenzhen 518055, China. [3]CAS Key Laboratory of Standardization and Measurement for Nanotechnology, CAS Center for Excellence in Nanoscience, National Centre for Nanoscience and Technology, Beijing 100190, China. ✉e-mail: hualu@mail.tsinghua.edu.cn; jingfeng@mail.tsinghua.edu.cn

temperature[17–19]. Moreover, the interest in interface engineering in $Mg_3(Sb,Bi)_2$ is growing, particularly focusing on the grain boundary engineering and two-phase interface engineering. On one hand, many strategies such as increasing sintering temperature[20], Mg-vapor annealing[15], and Cu[21] or Nb wetting phase[22] at grain boundaries, are employed to promote grain growth with the aim of optimizing the heterogeneity and electrical resistance of grain boundaries in $Mg_3(Sb,Bi)_2$[23,24]. However, this improvement is more pronounced at low temperatures probably due to the stronger carrier scattering at grain boundaries. On the other hand, by introducing highly conductive secondary phases, such as graphene nanoplatelets[25] and metal inclusions[26], at grain boundaries, the band structure at the grain boundaries can be bended, which helps to filter the low-energy electrons and enhance the electrical properties. Therefore, the introduction of highly conductive metal nanoparticles is expected to reduce the interfacial barrier in the $Mg_3(Sb,Bi)_2$ system.

Herein, high zT values of ~ 2.0 were obtained in $Mg_3(Sb,Bi)_2$ by incorporating built-in metallic nano-inclusions. Given the good wettability at the grain boundaries of $Mg_3(Sb,Bi)_2$, Nb was added into the $Mg_3Sb_{1.5}Bi_{0.49}Te_{0.01}$ matrix prepared by mechanical alloying (MA) combined with spark plasma sintering (SPS). The heterogeneous interfaces induced by the nano-sized Nb inclusions together with the grain size controlled by the high-temperature sintering strategy played vital roles in modulating the electrical transport properties. It was inferred that the embedded Nb inclusions at grain boundaries could

reduce the interfacial barriers, so the carriers can pass easily through the interfaces. Meanwhile, the S can be obviously enhanced in the $Mg_3(Sb,Bi)_2$ with Ta addition, indicating that these built-in metallic nano-inclusions effectively modified the interfacial barriers and enhanced the contribution from high-energy electrons to transport properties. Along with the diminished κ_L due to enhanced nanoparticle scattering, the zT values of $0.1Nb/Mg_3Sb_{1.5}Bi_{0.49}Te_{0.01}$ significantly increased to 0.80 at 300 K and 2.04 at 798 K, respectively. A conversion efficiency of 15% under $\Delta T = 470$ K was attained for the single-leg device, showing great commercial prospects in a wide temperature range (300–798 K).

Results

In general, both the carrier and phonon transports are significantly modulated by the Nb-rich secondary phases rather than Nb substitution. The electrical properties of the $xNb/Mg_3Sb_{1.5}Bi_{0.49}Te_{0.01}$ samples (Fig. 1) sintered at both the low and high temperatures show significant improvement after Nb addition, especially at 300–500 K. The near-room-temperature σ is positively correlated with sintering temperature and Nb content (Fig. 1a). Notably, the σ of $0.1Nb/Mg_3Sb_{1.5}Bi_{0.49}Te_{0.01}$ sintered at 1073 K is elevated to 7.6×10^2 S cm^{-1} at room temperature, showing 30% enhancement compared to the unadded sample. The σ of the $x = 0.2$ sample is even higher than that of the sample with $x = 0.1$. The absolute value of S increases with temperature but remains almost constant after Nb addition (Fig. 1b).
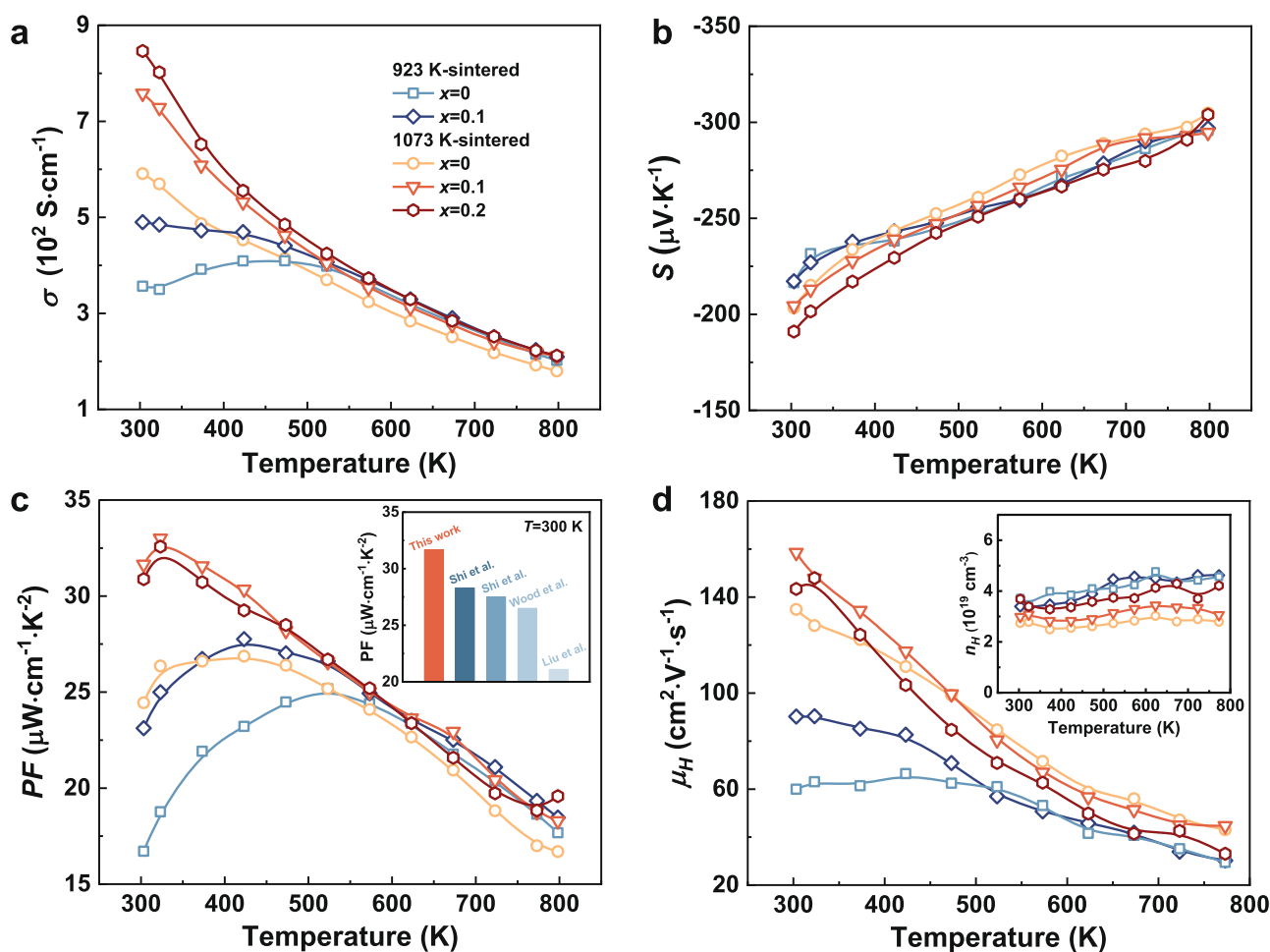

Fig. 1 | The electrical transport properties of Nb-added samples. a Temperature dependence of electrical conductivity. **b** Temperature dependence of Seebeck coefficient. **c** Temperature dependence of PF for $xNb/Mg_3Sb_{1.5}Bi_{0.49}Te_{0.01}$ ($x = 0$, 0.1 and 0.2) sintered at 923 K and 1073 K. The inset of **c** shows the comparison of PF in this work with previously reported results[15,21,27,28]. **d** Temperature dependence of Hall mobility for $xNb/Mg_3Sb_{1.5}Bi_{0.49}Te_{0.01}$ ($x = 0$, 0.1 and 0.2). The inset of **d** shows the temperature dependence of carrier concentration.

However, a slight decrease in S is observed at low temperatures in the $x = 0.2$ sample. Due to the highly enhanced σ with negligible changes to S, a high PF (over 31 μW cm^{-1} K^{-2}) is obtained in 0.1Nb/Mg$_3$Sb$_{1.5}$Bi$_{0.49}$Te$_{0.01}$ at room temperature, as shown in Fig. 1c; this value ranks the highest among the data reported for Mg$_3$(Sb,Bi)$_2$[15,21,27,28] in earlier studies. Essentially, the S contributes more to the high PF while the σ is comparable to the values reported in other literatures, as demonstrated in Supplementary Fig. 1. The electrical properties of the sample with $x = 0.05$ and 0.15 are also shown in Supplementary Fig. 2. Clearly, with Nb addition, the temperatures corresponding to the highest σ and PF also shift towards lower values, representing the optimization of electrical transport performance at low temperatures.

To provide clear insights into the superior electrical transport properties, the Hall carrier concentration (n_H) and mobility (μ_H) were measured (Fig. 1d). The results of Hall measurement suggest that the μ_H of the $x = 0.1$ sample shows a remarkable increase at low temperatures, whereas this enhancement is obviously weakened above 450 K. Meanwhile, all the Nb-added samples sintered at 1073 K show enhanced n_H within the entire temperature range compared to the unadded sample; the n_H increases with increasing Nb content. Due to the increased n_H, the carrier scattering is enhanced, resulting in a decrease in μ_H for 0.2Nb/Mg$_3$Sb$_{1.5}$Bi$_{0.49}$Te$_{0.01}$. The weighted mobility (μ_W) is also calculated, shown in Supplementary Fig. 3. The $x = 0.2$ sample maintains a high μ_W similar to that of $x = 0.1$, demonstrating noteworthy improvement compared to the unadded sample. On the contrary, the variation trend of n_H with Nb content is different for the samples sintered at 923 K. In fact, the changes in n_H and μ_H cannot be solely ascribed to the variable point defects (e.g. Mg vacancies[29] or doping atoms[27]) as thought conventionally, because the carrier scattering induced by point defects is usually more intense in the high-temperature range, which significantly affects the electrical properties at high temperatures. Mostly, the increased n_H leads to a lower S. But there is an inconsistency between the trend of the S and n_H for the 1073 K-sintered samples. This may be attributed to the reduced interfacial barriers allowing more high-energy carriers to contribute to the S (this will be anatomized later). Therefore, a higher S is still observed in $x = 0.1$ sample with an increased n_H. In general, according to $\sigma = n_H e \mu_H$, where e is the electronic charge, the increased n_H and μ_H contribute in tandem to enhancing σ. As a result, Nb addition not only provides extra electrons but also enhances μ_H near room temperature. By contrast, the reduced mobility at high temperatures is probably assigned to the enhanced electron scattering. Meanwhile, the slight decrease in S mainly stems from the increased n_H. Similarly, a more pronounced decrease in S is observed due to higher n_H in the $x = 0.2$ sample. Nevertheless, the augmented electron concentration donated by Nb still guarantees higher σ (a 17% increase at 798 K), leading to enhanced PF at high temperatures. This might be ascribed to a small amount of Sb atoms being consumed from the matrix caused by the formation of Nb$_3$Sb phase.

The enhanced charge carrier transport is closely associated with microstructures. As shown in Fig. 2a, the grain size of the 923 K-sintered samples is estimated to be about 2 μm. The grain growth seems insensitive to Nb addition (Fig. 2a, b), but the σ at room temperature is improved. For the 1073 K-sintered samples (Fig. 2c, d), the grain size increases more than threefold in value (~7.2 μm), compared to that of the 923 K-sintered samples. Interestingly, by elevating sintering temperature, only a slighter increase in grain size (from 2.3 to 3.7 μm) was observed for the $x = 0.1$ sample. In spite of smaller grain size, the μ_H of the Nb-added samples is still retained a high level (158.4 cm^2 V^{-1} s^{-1}), even higher than that of the unadded samples (134.8 cm^2 V^{-1} s^{-1}). This result conflicts with the conventional view that the room-temperature σ increases with grain size, because of the reduced density of electrically resistive grain boundaries[15,20,24]. The smaller grain size in the Nb-added samples sintered at 1073 K contributes to enhancing the grain boundary resistance, but the presence of Nb
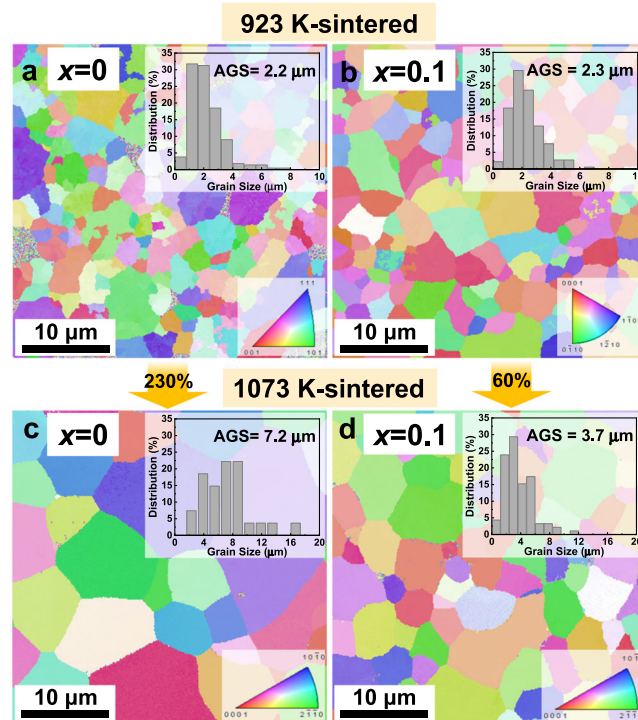

Fig. 2 | Grain size evolution induced by Nb inclusions. Electron backscatter diffraction (EBSD) crystal-orientation maps of xNb/Mg$_3$Sb$_{1.5}$Bi$_{0.49}$Te$_{0.01}$ ($x = 0$ and 0.01) sintered at 923 K (**a**, **b**) and 1073 K (**c**, **d**). The insets are the corresponding statistics on the grain size distribution.

inclusion is able to cancel the negative effect of grain boundaries on electrical properties near room temperature. As shown in the X-ray diffraction (XRD) patterns (Supplementary Fig. 4), extra Bragg reflection peaks are detected at 38.4° in the Nb-added samples. The energy-dispersive X-ray spectroscopy (EDS) elemental mapping on the fracture surface (Supplementary Fig. 5) also confirms the existence of Nb-rich secondary phases in the Nb-added samples. The Nb inclusion is further investigated by a microscope equipped with an EDS detector in the C_s-corrected high-angle annular dark-field scanning transmission electron microscopy (HAADF-STEM) mode (Fig. 3a–e). It is found that the Nb-rich secondary phases distribute randomly at grain boundaries. The atomic ratios of the central region of the Nb inclusion are shown in Fig. 3f, matching well with the chemical composition of Mg$_{4.5}$Nb$_{86.0}$Sb$_{9.5}$. Furthermore, the EDS analysis also indicates that the Nb atoms do not enter the lattice of the matrix, as shown in Supplementary Fig. 6. More Nb-rich inclusions, about ten to hundreds of nanometers in diameter, are observed in Supplementary Fig. 7. These inclusions help to pin grain boundaries, hindering grain boundary migration and suppressing grain growth.

Back to the question: how does Nb benefit the electrical transport? Considering the facts that increased grain boundaries enhance the interface resistance and Nb inclusions increase the number of interfaces, it is not difficult to infer that the interfaces between Nb and matrix should own lower resistance than the grain boundaries. Therefore, the embedded Nb inclusions at grain boundaries should help to reduce the interfacial barriers and weaken the grain boundary scattering, which promotes carrier transport, as schematically shown in Fig. 3g. Essentially, it may be derived from the weak interface scattering due to the good wettability of Nb to the grains[22]. It is known that interface scattering is more effective in the low-temperature range. This also explains why the improvement in μ_H becomes negligible in the high-temperature range. In addition, the resulting metal-semiconductor interfaces modulate the scattering mechanisms. In
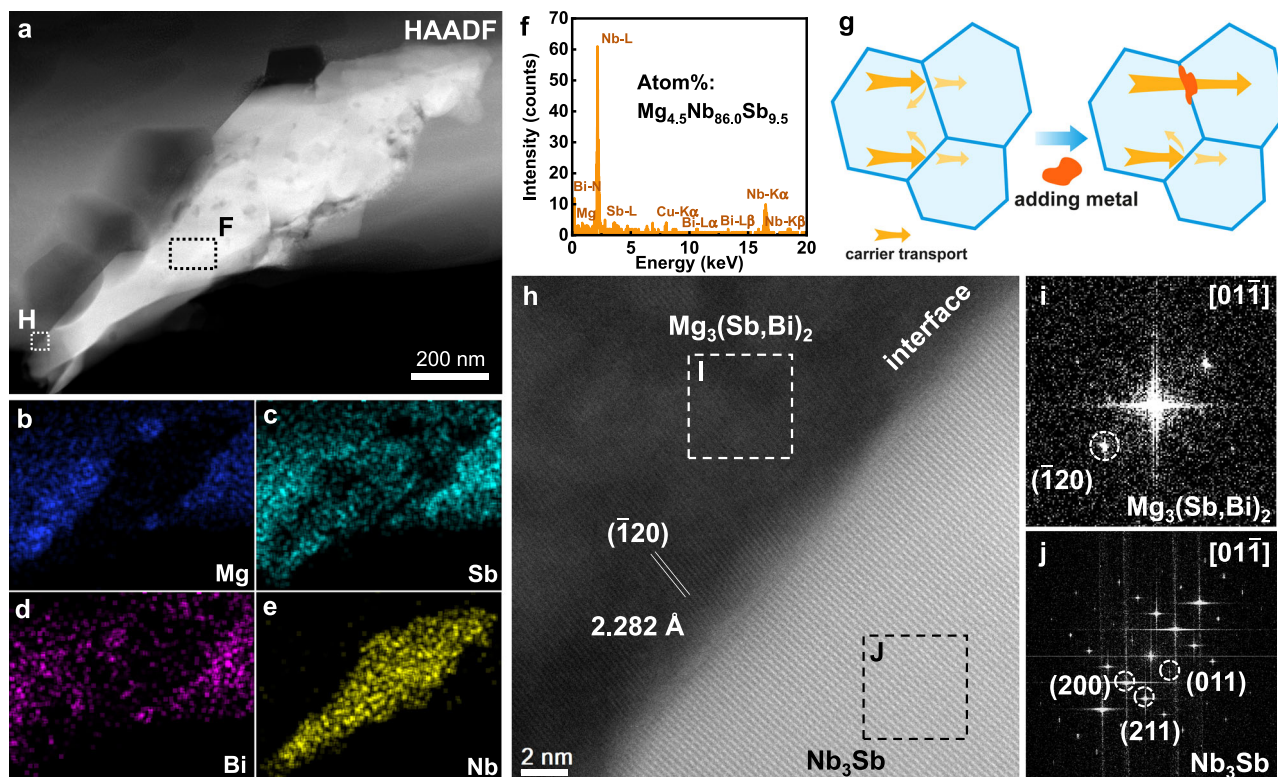
Fig. 3 | Microstructure and interface analysis. a HAADF-STEM mapping of 0.1Nb/$Mg_3Sb_{1.5}Bi_{0.49}Te_{0.01}$ sintered at 1073 K, and corresponding EDS maps for (**b**) Mg, (**c**) Sb, (**d**) Bi and (**e**) Nb. **f** EDS analysis for a Nb-rich secondary phase inclusion from a random region F in **a**. **g** Schematic illustration of different carrier transport behaviors at grain boundaries and metallic inclusions. **h** An HRTEM image of the interface between the matrix and Nb-rich secondary phase from the region H in **a** with the (**i**) FFT image of the boxed region I and (**j**) FFT image of region J in **h**.

0.1Nb/$Mg_3Sb_{1.5}Bi_{0.49}Te_{0.01}$, the absolute value of the temperature exponent derived from the Hall mobility is higher than that of the matrix. It indicates that the grain boundary scattering mechanism is partially involved for the large-grain samples. The modified interfacial effect by metallic inclusions cancels the decrease in mobility caused by grain boundary scattering, making the acoustic phonon scattering dominant. Figure 3h presents the high-resolution transmission electron microscopy (HRTEM) image of the interface between the matrix and Nb inclusions. The corresponding fast Fourier transform (FFT) patterns (Fig. 3i, j) illustrate the crystal structures of $Mg_3(Sb,Bi)_2$ and Nb_3Sb viewed in the [01$\bar{1}$] zone axis. The Nb-Sb binary phase diagram can serve as evidence for the presence of stable Nb_3Sb phase (Supplementary Fig. 8a)[30]. However, no peaks of the Nb_3Sb phase are observed in the XRD patterns (Supplementary Fig. 4), indicating that only a small amount of Nb_3Sb is formed at the interface. The Sb in the matrix may diffuse to the Nb inclusion, leading to the formation of new secondary phases near the interfaces. The Nb_3Sb phase has a resistivity of 7×10^{-7} Ω m at 298 K[31], which is slightly higher than the value of 1.6×10^{-7} Ω m for Nb metal[32] but much lower than that of the matrix. These composition-transition interfaces with high conductivity further support the modulation of interfacial barriers by Nb inclusions. Similar interfacial structures between the matrix and the metallic inclusions are displayed in Supplementary Fig. 9. The inclusions perhaps have a core-shell-like structure with Nb as the main body and a small amount of Nb_3Sb as the coating layer, as demonstrated in Supplementary Fig. 8b. As there is no orientation relationship between the Nb_3Sb phase and the matrix, the Nb-rich inclusions are unlikely to be in situ informed. The modulation of the scattering mechanisms by Nb inclusions remarkably improves the mobility. Besides, due to the formation of the Nb_3Sb phase near the interface, a small amount of Sb atoms in the matrix would be inevitably consumed by Nb. As shown in

Supplementary Fig. 10, the results of electron probe microanalysis (EPMA) confirmed that the atomic ratio of Sb/Mg in the matrix of $x = 0.1$ sample is lower than that of the unadded sample. The decreased Sb/Mg ratio may suppress the formation of Mg vacancies, which is beneficial to increasing the n_H and hence the σ of $Mg_3(Sb,Bi)_2$. Moreover, the investigation of the Nb/Mg_3SbBi interface also confirms that Nb is in good contact with the matrix without macroscopic secondary phases[33,34].

The Nb nano-inclusions not only influence the carrier transport but also interact with phonons. The temperature dependence of total and lattice thermal conductivity is shown in Fig. 4a and Supplementary Fig. 2. The κ and κ_L decrease first and then increase upon the addition of Nb. A relatively low κ of 0.45 W m^{-1} K^{-1} is obtained for 0.1Nb/$Mg_3Sb_{1.5}Bi_{0.49}Te_{0.01}$ sintered at 1073 K. On one hand, the κ and κ_L are significantly reduced due to the abundant vacancies and vacancy clusters as a consequence of the loss of volatile elements at high sintering temperatures (detailed discussion is provided in our previous work)[35]. On the other hand, the κ_L is further reduced by nanoparticle scattering. The sizes of Nb secondary phase are averaged about 200 nm in diameter but are distributed from 10 to 1000 nm, which cover a large range of phonon mean free paths. The variable κ_L is probably related to the different interfacial thermal resistance originating from the layered or granular bonding between metal and matrix. Notably, it was reported that the κ increased when the thin wetting Nb layer was formed at grain boundaries[22]. In this case, the two-phase model equivalent to a one-dimensional series circuit can be utilized to understand the increase in κ[24], which probably stems from the reduction in interfacial thermal resistance. When Nb exists in the form of secondary phases (from nano to sub-micron scales), the additional scattering centers induced by these nano-inclusions contribute to the reduction in κ_L by suppressing the propagation of
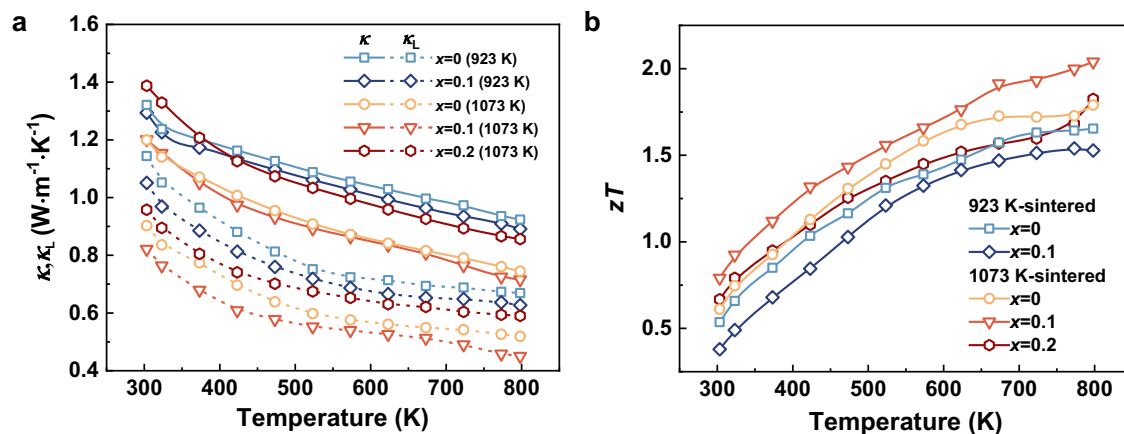
Fig. 4 | Thermal conductivity and figure-of-merit zT of Nb-added samples. Temperature dependence of (**a**) total thermal conductivity and lattice thermal conductivity, and (**b**) zT values for xNb/Mg$_3$Sb$_{1.5}$Bi$_{0.49}$Te$_{0.01}$ sintered at 923 K and 1073 K.

phonons. However, the κ significantly increases when the amount of Nb increases to more than 0.1; higher fractions of thermally conducting Nb phases are more likely to affect the κ through its intrinsic nature. When the contribution from the high κ of Nb phase (53.7 W m^{-1} K^{-1}) overweighs the reduction in κ by phonon scattering, the κ and κ_L will rise. Moreover, due to the more pronounced Mg volatilization during high-temperature sintering, no Mg-rich phase is observed in the unadded and Nb-added samples, which is confirmed by the EDS analysis (Supplementary Figs. 5 and 11), excluding the effect of excessive Mg on κ. The total TE performance is enhanced by Nb nano-inclusions in conjunction with high-temperature sintering, as shown in Fig. 4b. The room-temperature zT value increases from 0.38 to 0.80 and the peak zT value is elevated from 1.53 to 2.04 for 0.1Nb/Mg$_3$Sb$_{1.5}$Bi$_{0.49}$Te$_{0.01}$ due to the increased PF and reduced κ, showing ~110% and 33% enhancement, respectively. Moreover, the TE properties of the as-prepared samples exhibit good repeatability, which can be confirmed by the data in Supplementary Fig. 12.

Furthermore, since Nb and tantalum (Ta) are mainly found in tantalite and are symbiotic with each other, the Ta is expected to exhibit similar behaviors. As expected, similar enhancement in the TE performance was discovered in the Ta-added Mg$_3$(Sb,Bi)$_2$ sintered at 1073 K. Figure 5a depicts the temperature-dependent electrical conductivity and Seebeck coefficient of 0.1Nb/Mg$_3$Sb$_{1.5}$Bi$_{0.49}$Te$_{0.01}$ and 0.1Ta/Mg$_3$Sb$_{1.5}$Bi$_{0.49}$Te$_{0.01}$ prepared under the same conditions. Different from the significant increase after Nb addition, the σ only increases slightly after Ta addition. Yet it is worth noting that the S increases with Ta addition, especially at high temperatures. Based on the simultaneous optimization of σ and S, the PF of 0.1Ta/Mg$_3$Sb$_{1.5}$Bi$_{0.49}$Te$_{0.01}$ is up to 32 μW cm^{-1} K^{-2} at 323 K and close to 20 μW cm^{-1} K^{-2} at 798 K, as shown in Fig. 5b. Interestingly, the improvement in electrical properties near room temperature is the same as the case relevant to Nb but less dramatic, while the effect of Ta becomes more pronounced at high temperatures. As shown in Supplementary Table 1, both n_H and μ_H of the Ta-added sample slightly increase at room temperature, but are less than the values of the Nb-added sample. Similar to the Nb-added samples, nanoscale Ta metal inclusions randomly distribute at grain boundaries in 0.1Ta/Mg$_3$Sb$_{1.5}$Bi$_{0.49}$Te$_{0.01}$, as demonstrated in Supplementary Figs. 13–15. The reason may be that both Nb and Ta are refractory and have good chemical stability. The scanning electron microscope (SEM) images of the fracture surfaces shown in Supplementary Fig. 16 display the grain size of Nb-added and Ta-added samples. The grain size of the Ta-added sample approximately decreases to the level of that of the Nb-added samples, which is also attributed to the pinning effect of inclusions at grain boundaries. The embedded Ta nano-inclusions at grain

boundaries should have the similar effect as Nb. However, no Ta-rich secondary phases similar to Nb$_3$Sb were formed under the present experimental conditions; in fact, that no Ta-Sb binary phase diagram was reported might account for why the Ta addition did not affect the carrier concentration as in the case of the Nb-added samples.

Benefiting from the marginally increased n, the contribution to the S from the inclusions becomes easier to distinguish. The built-in Nb/Ta nano-inclusions may scatter the low-energy carriers more efficiently via modifying the interfacial barriers[36,37]. As mentioned above, the secondary phases near the interface would reduce interfacial potential barriers. It is speculated that these barriers of metal-semiconductor interfaces are lower than that of Mg-deficient grain boundaries, as demonstrated in Fig. 5c. The higher barriers at grain boundaries (E_{b1}) in the unadded samples would block low-energy and part of high-energy carriers. By incorporating Ta inclusions, the interfacial barrier is reduced from E_{b1} to E_{b2}, allowing more high-energy carriers to pass through. The contribution from high-energy carriers to transport properties is enhanced, giving rise to a higher S. In the case for Nb-added samples, this modified interfacial barrier turns out to optimize σ without sacrificing S, thereby leading to enhanced PF. The S may be a synergistic result of the above effect and increased n_H. The Pisarenko plots shown in Supplementary Fig. 17 exhibit the contribution from the modified interfacial barrier to S, where the data points deviate upward slightly. Recently, it has been reported that the Mo addition also increases the σ of Mg$_3$(Sb,Bi)$_2$-based materials[38], indicating the great potential of other transition metals. However, the enhanced σ by Mo addition is mainly due to the grain boundary effect, different from those analyzed above for the Nb or Ta inclusions.

The incorporation of Nb and Ta nano-inclusions into the Mg$_3$(Sb,Bi)$_2$ matrix helps to modify the interfacial barriers, producing similar favorable modulation results. As a consequence of the optimized electrical performance, a high zT value of 2.06 is obtained in 0.1Ta/Mg$_3$Sb$_{1.5}$Bi$_{0.49}$Te$_{0.01}$ at 798 K, as shown in Fig. 6a. However, due to the higher κ (57.5 W m^{-1} K^{-1}) as well as weaker phonon scattering originating from the larger size of Ta inclusions, the effect of Ta inclusions on reducing κ is limited (Supplementary Fig. 18). The zT values of Ta-added samples within the low- and middle-temperature range are slightly lower than that of Nb-added samples. After adding these metallic inclusions into the matrix, the zT values increase over the entire temperature range, thereby boosting the average zT value (zT_{ave}) calculated using the following formula:

$$zT_{ave} = \frac{\int_{T_c}^{T_h} zT\,dT}{T_h - T_c} \tag{1}$$

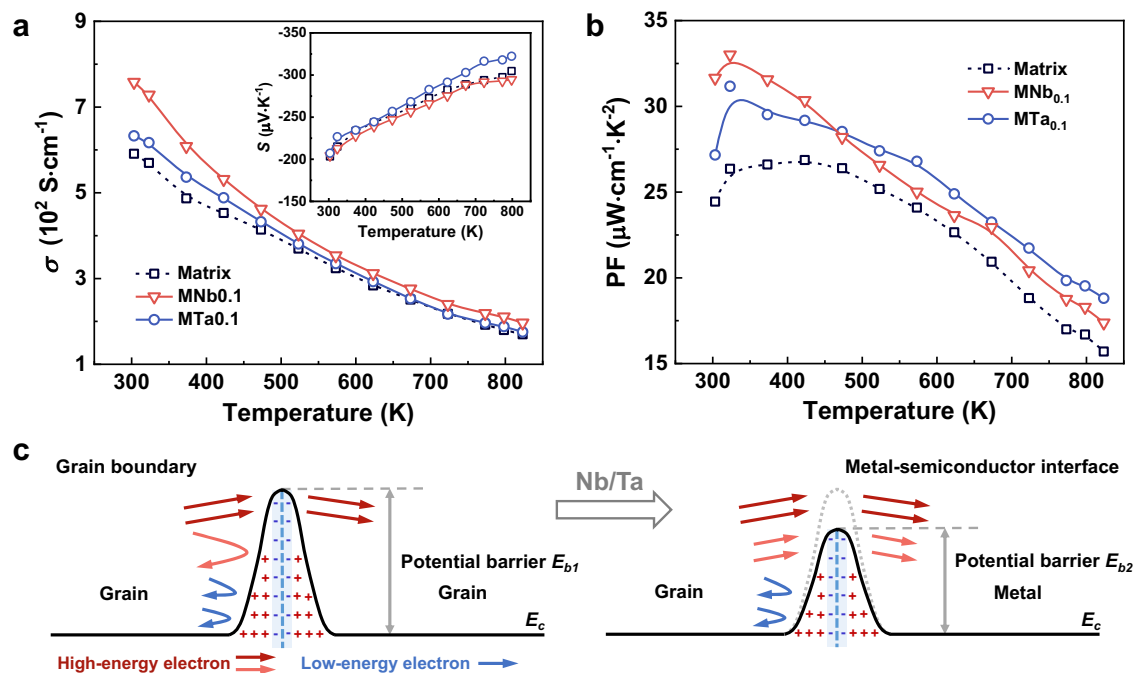**Fig. 5 | The electrical transport properties of Ta-added samples and illustration of the modified interfacial barrier.** Temperature dependence of (**a**) electrical conductivity and Seebeck coefficient and (**b**) PF for $0.1Nb/Mg_3Sb_{1.5}Bi_{0.49}Te_{0.01}$ and $0.1Ta/Mg_3Sb_{1.5}Bi_{0.49}Te_{0.01}$. **c** Schematic illustration of interfacial barriers near the grain boundary region and metal-semiconductor interface region; E_b is the interfacial potential barrier and E_c is the energy of the conduction band minimum.

where T_h and T_c are the temperatures of the hot side and cold side, respectively. The zT_{ave} values reach 1.57 and 1.51 within the temperature range of 300–798 K for $0.1Nb/Mg_3Sb_{1.5}Bi_{0.49}Te_{0.01}$ and $0.1Ta/Mg_3Sb_{1.5}Bi_{0.49}Te_{0.01}$, respectively. The zT_{ave} values of the Nb-added sample in the temperature range 300–773 K and 300–573 K are also calculated, which are 1.54 and 1.30, respectively. Compared to the previously reported results for $Mg_3(Sb,Bi)_2$, the zT_{ave} values are at the state-of-the-art level and even superior to $Bi_2(Te,Se)_3$, which is competitive near room temperature (Fig. 6b)[20,27,39–43]. Based on such a high TE performance for the optimized sample, i.e. $0.1Nb/Mg_3Sb_{1.5}Bi_{0.49}Te_{0.01}$ sintered at 1073 K, a single-leg device was fabricated with the Fe_7Mg_2Cr interface and sintered copper electrode to evaluate the TE energy conversion efficiency. As shown in Fig. 6c and Supplementary Fig. 19, a high efficiency of around 15% is obtained for a single leg under a ΔT of 470 K. The excellent reproducibility of the efficiency measured by the single legs is shown in Supplementary Figs. 20 and 21. The theoretical efficiency of the single-leg device reaches 18% as shown in Supplementary Fig. 22, but both the measured output power and heat flow deviate from the predicted value, indicating additional efforts are needed to optimize the contact layer and control the thermal radiation. In addition, a continuous measurement on the output properties (the inset of Fig. 6d and Supplementary Fig. 23) reveals that the single leg can operate over 120 h at a $\Delta T = 470$ K with an efficiency higher than 14%, showing good service stability. Figure 6d exhibits the high-efficiency values reported in $Mg_3(Sb,Bi)_2$ system in recent years, indicating the efficiency achieved in this work rivals other multiple-leg modules but has a wider application temperature range. It is worth noting that, due to the promoted electrical transport by the metallic nano-inclusions, a competitive value is obtained in the low-temperature range, surpassing that of the classical bismuth telluride with broad prospects for commercial applications in electronic cooling.

Discussion

In summary, a high peak zT value of 2.04 at a relatively low temperature (798 K) and a remarkable zT_{ave} (300–798 K) of 1.57 for

$Mg_3(Sb,Bi)_2$ were reported in this work. The fabricated single-leg device showed a high TE conversion efficiency of ~15%, which rivaled those of well-designed modules. The significantly improved TE performance was attributed to the modulation of charge carriers and phonons transport via introducing Nb/Ta inclusions at grain boundaries. The reduced interfacial barriers significantly increased the electrical conductivity in the low-temperature range. Besides, the Nb and Ta inclusions not only contributed to increasing n_H but also led to remarkably enhanced μ_H near room temperature. As a result, the PF was significantly increased, especially at low temperatures. Combined with the effective phonon scattering effect caused by a small number of metallic inclusions, the lattice thermal conductivity was also obviously diminished. Our findings provide a new strategy to deal with the high grain boundary resistance in $Mg_3(Sb,Bi)_2$-based materials, particularly demonstrating great potential in near-room-temperature applications.

Methods

Synthesis

Magnesium turnings (99.9%), antimony shots (99.999%), bismuth shots (99.999%), tellurium powder (99.999%), niobium powder (99.9%, 325 mesh) and tantalum powder (99.9%, 325 mesh) were weighed in accordance with the nominal stoichiometry of $Mg_{3.2}Sb_{1.5}Bi_{0.49}Te_{0.01}$ and $Mg_{3.1}X_{0.1}Sb_{1.5}Bi_{0.49}Te_{0.01}$ (X = Nb and Ta) and then ball-milled for 8 h in the SPEX 8000D Mixer/Mill ball mill (SPEX, Metuchen, NJ, United States). To explore the effect of Nb on electrical transport properties, the powder with the composition of $Mg_{3.1}Nb_xSb_{1.5}Bi_{0.49}Te_{0.01}$ (x = 0.05, 0.15, and 0.2) was also prepared. The ball-milled powder was sintered by spark plasma sintering using the SPS 211Lx Spark Plasma Sintering Machine (Fuji Electronic Industrial Co., Tsurugashima, Saitama, Japan) at 923 K and 1073 K for 20 min under an axial pressure of 50 MPa. To fabricate the single-leg device, the sintered bulk, TE interface material (TEiM) powders and Cu powders (99.9%) were sandwiched in a graphite die and then sintered at 873 K for 10 min under a pressure of 50 MPa. The TEiM powders were generated by ball milling after mixing Fe powder (99.9%), Mg turnings
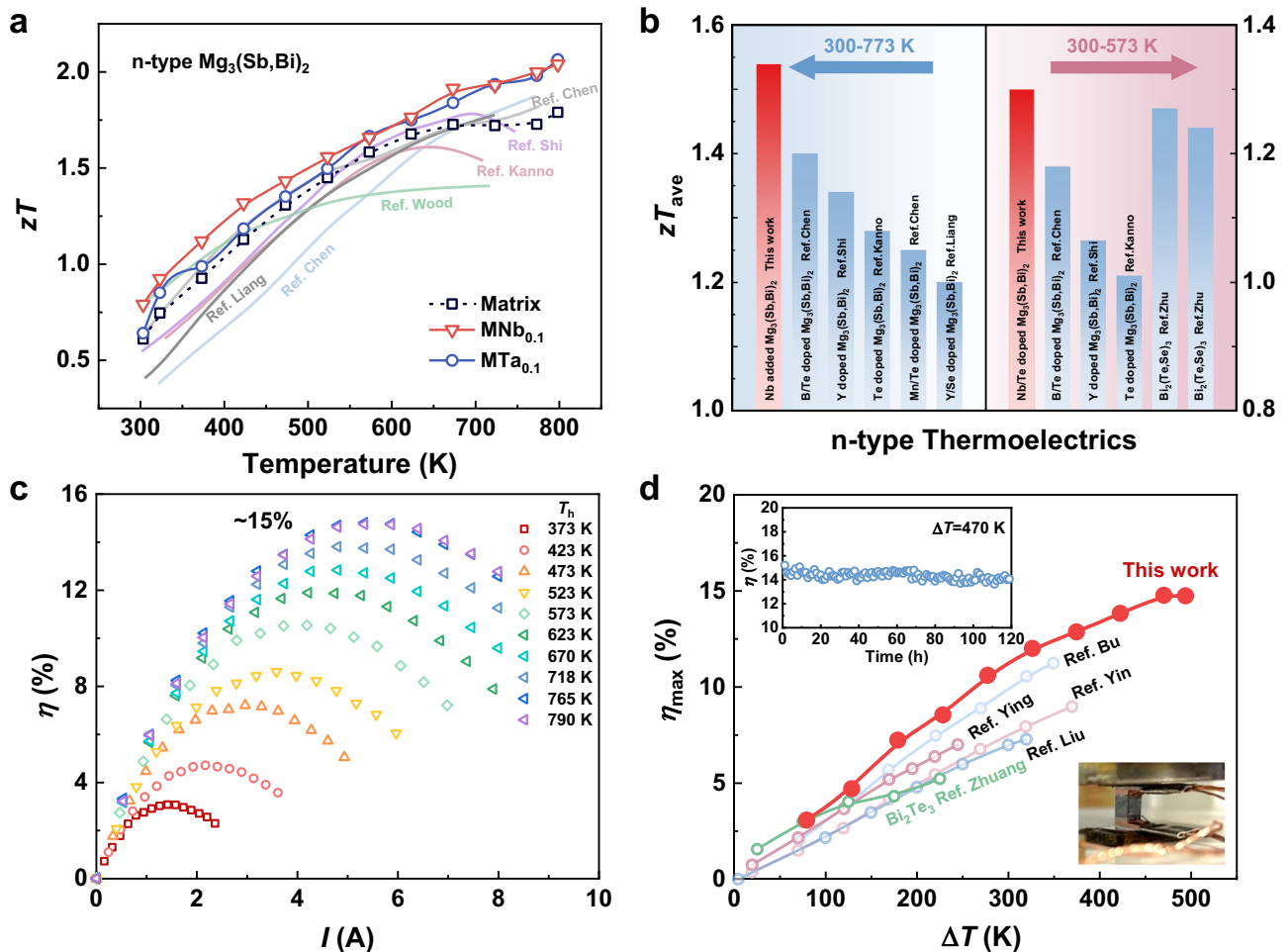
Fig. 6 | Comparison of figure-of-merit *zT* and conversion efficiency with previous studies. a Temperature dependence of *zT* values for 0.1Nb/ $Mg_3Sb_{1.5}Bi_{0.49}Te_{0.01}$ and 0.1Ta/$Mg_3Sb_{1.5}Bi_{0.49}Te_{0.01}$ in comparison with the state-of-the-art n-type $Mg_3(Sb,Bi)_2$[15,20,27,39–41]. **b** Comparison of average *zT* in the temperature range of 300–773 K and 300–573 K for 0.1Nb/$Mg_3Sb_{1.5}Bi_{0.49}Te_{0.01}$ and other n-type thermoelectrics[20,27,39–43]. **c** The measured conversion efficiency of the single-leg device in the temperature range of 373–790 K and the cold side temperature is 295 K. **d** Comparison of the maximum conversion efficiency among the single-leg device in this work, other $Mg_3(Sb,Bi)_2$ modules, and Bi_2Te_3 module under a series of temperature difference (ΔT)[21,45–48]. The inset in **d** is the optical image of the fabricated TE single-leg device in this work and the time-dependent efficiency for the single-leg device under $\Delta T = 470$ K.

(99.9%), and Cr powder (99.5%). The thicknesses of the sintered bulk and TEiM layers were 8 and 1.5 mm, respectively.

Characterization

The phase purity of the material was determined by powder X-ray diffraction (XRD) using the Bruker D8 Advance X-ray diffractometer (Bruker AXS GmbH, Karlsruhe, Germany) with Cu-Kα radiation. The grain size and crystal orientation were determined via electron backscatter diffraction (EBSD) by the ULVAC-PHI 710 Scanning Auger spectrometer (ULVAC-PHI, Inc., Chigasaki, Japan). Scanning transmission electron microscopy (STEM) observations were performed on the Spectra 300 double-C_s-corrected transmission electron microscope (Thermo Fisher Scientific Inc.) equipped with a field-emission electron source, operating at an accelerating voltage of 300 kV. Atomic resolution energy-dispersive X-ray spectroscopy (EDS) elemental mapping and analysis were conducted using the Super-X EDS detector. The morphology and microstructure were characterized by field-emission scanning electron microscopy (FESEM, Zeiss Merlin, Germany). The fracture surface morphology and elemental distribution were characterized by field-emission scanning electron microscope (FE-SEM, Gemini 2, Zeiss, Germany) equipped with an EDS detector. The quantitative analysis of

elements was studied via electronic probe microscopic analysis (JXA-8230, JEOL, Japan).

Thermoelectric property measurements

The Seebeck coefficient (*S*) and conductivity (σ) were determined using a ZEM-3 Seebeck coefficient/electric resistance measuring system (ULVAC-RIKO Inc., Yokohama, Japan). Thermal conductivity (κ) was calculated using the equation $\kappa = DC_p\rho$, where the thermal diffusivity (*D*) was measured with the LFA 457 laser flash apparatus (Netzsch GmbH, Selb, Germany). The specific heat capacity (C_p) was derived using the Dulong–Petit law, and the density (ρ) was measured in accordance with the Archimedes method. The electronic thermal conductivity (κ_e) was calculated based on the Wiedeman–Franz law ($\kappa_e = \sigma LT$), where the Lorenz factor (*L*) was estimated using the equation $L = 1.5 + \exp(-\frac{|S|}{116})$[44]. The Hall coefficient (R_H) was determined using the Hall measurement system (ResiTest 8340DC, Tokyo, Japan). The Hall carrier concentration (n_H) and mobility (μ_H) were calculated using the equations $n_H = 1/(eR_H)$ and $\mu_H = \sigma R_H$, respectively. The conversion efficiency (η) of the single-leg device was calculated in accordance with the equation $\eta = P/(P + Q_c) \times 100\%$, where the output power (*P*) and cold side heat flow (Q_c) were simultaneously measured with the Mini-PEM testing

system (Ulvac-Riko, Japan). The theoretical conversion efficiency was simulated using the COMSOL Multiphysics software.

Data availability

The data that support the findings of this study are available from the corresponding author on request.

References

1. Bell, L. E. Cooling, heating, generating power, and recovering waste heat with thermoelectric systems. *Science* **321**, 1457–1461 (2008).
2. Snyder, G. J. & Toberer, E. S. Complex thermoelectric materials. *Nat. Mater.* **7**, 105–114 (2008).
3. Pei, Y. et al. Convergence of electronic bands for high performance bulk thermoelectrics. *Nature* **473**, 66–69 (2011).
4. Biswas, K. et al. High-performance bulk thermoelectrics with all-scale hierarchical architectures. *Nature* **489**, 414–418 (2012).
5. Zhao, L.-D. et al. Ultralow thermal conductivity and high thermoelectric figure of merit in SnSe crystals. *Nature* **508**, 373–377 (2014).
6. Chang, C. et al. 3D charge and 2D phonon transports leading to high out-of-plane ZT in n-type SnSe crystals. *Science* **360**, 778–783 (2018).
7. Liu, H. et al. Copper ion liquid-like thermoelectrics. *Nat. Mater.* **11**, 422–425 (2012).
8. Zhao, K. et al. Solid-state explosive reaction for nanoporous bulk thermoelectric materials. *Adv. Mater.* **29**, 1701148 (2017).
9. Pan, Y. et al. Melt-centrifuged $(Bi,Sb)_2Te_3$: engineering microstructure toward high thermoelectric efficiency. *Adv. Mater.* **30**, 1802016 (2018).
10. Zhuang, H.-L. et al. High ZT in p-type thermoelectric $(Bi,Sb)_2Te_3$ with built-in nanopores. *Energy Environ. Sci.* **15**, 2039–2048 (2022).
11. Qin, B. et al. Power generation and thermoelectric cooling enabled by momentum and energy multiband alignments. *Science* **373**, 556–561 (2021).
12. Tan, X. Y. et al. Enhanced near-room-temperature thermoelectric performance in GeTe. *Rare Metals* **41**, 3027–3034 (2022).
13. Tamaki, H., Sato, H. K. & Kanno, T. Isotropic conduction network and defect chemistry in $Mg_{3+\delta}Sb_2$-based layered zintl compounds with high thermoelectric performance. *Adv. Mater.* **28**, 10182–10187 (2016).
14. Zhang, J. et al. Discovery of high-performance low-cost n-type Mg_3Sb_2-based thermoelectric materials with multi-valley conduction bands. *Nat. Commun.* **8**, 13901 (2017).
15. Wood, M., Kuo, J. J., Imasato, K. & Snyder, G. J. Improvement of low-temperature zT in a Mg_3Sb_2–Mg_3Bi_2 solid solution via Mg-vapor annealing. *Adv. Mater.* **31**, 1902337 (2019).
16. Shu, R. et al. $Mg_{3+\delta}Sb_xBi_{2-x}$ family: a promising substitute for the state-of-the-art n-type thermoelectric materials near room temperature. *Adv. Funct. Mater.* **29**, 1807235 (2019).
17. Mao, J. et al. High thermoelectric cooling performance of n-type Mg_3Bi_2-based materials. *Science* **365**, 495–498 (2019).
18. Imasato, K., Kang, S. D., Ohno, S. & Snyder, G. J. Band engineering in Mg_3Sb_2 by alloying with Mg_3Bi_2 for enhanced thermoelectric performance. *Mater. Horiz.* **5**, 59–64 (2018).
19. Han, Z. et al. The electronic transport channel protection and tuning in real space to boost the thermoelectric performance of $Mg_{3+\delta}Sb_{2-y}Bi_y$ near room temperature. *Research* **2020**, 1–12 (2020).
20. Kanno, T. et al. Enhancement of average thermoelectric figure of merit by increasing the grain-size of $Mg_{3.2}Sb_{1.5}Bi_{0.49}Te_{0.01}$. *Appl. Phys. Lett.* **112**, 033903 (2018).
21. Liu, Z. et al. Demonstration of ultrahigh thermoelectric efficiency of ~7.3% in Mg_3Sb_2/MgAgSb module for low-temperature energy harvesting. *Joule* **5**, 1196–1208 (2021).
22. Luo, T. et al. Nb-mediated grain growth and grain-boundary engineering in Mg_3Sb_2-based thermoelectric materials. *Adv. Funct. Mater.* **31**, 2100258 (2021).
23. Kuo, J. J. et al. Mg deficiency in grain boundaries of n-Type Mg_3Sb_2 identified by atom probe tomography. *Adv. Mater. Interfaces* **6**, 1900429 (2019).
24. Kuo, J. J. et al. Grain boundary dominated charge transport in Mg_3Sb_2-based compounds. *Energy Environ. Sci.* **11**, 429–434 (2018).
25. Lin, Y. et al. Expression of interfacial Seebeck coefficient through grain boundary engineering with multi-layer graphene nanoplatelets. *Energy Environ. Sci.* **13**, 4114–4121 (2020).
26. Zhao, W. et al. Superparamagnetic enhancement of thermoelectric performance. *Nature* **549**, 247–251 (2017).
27. Shi, X. et al. Extraordinary n-type Mg_3SbBi thermoelectrics enabled by yttrium doping. *Adv. Mater.* **31**, 1903387 (2019).
28. Shi, X. et al. Efficient Sc-doped $Mg_{3.05-x}Sc_xSbBi$ thermoelectrics near room temperature. *Chem. Mater.* **31**, 8987–8994 (2019).
29. Shuai, J. et al. Significant role of mg stoichiometry in designing high thermoelectric performance for $Mg_3(Sb,Bi)_2$-based n-type zintls. *J. Am. Chem. Soc.* **140**, 1910–1915 (2018).
30. Lomnytska, Ya. F. & Kuz'ma, Yu. B. The Nb–Sb system. *J. Alloy. Compd* **413**, 114–117 (2006).
31. Arko, A. J., Fisk, Z. & Mueller, F. M. de Haas-van Alphen effect and Fermi surface of Nb_3Sb. *Phys. Rev. B* **16**, 1387–1392 (1977).
32. Cox, W. R., Hayes, D. J. & Brotzen, F. R. Temperature dependence of the hall effect and resistivity in single crystals of Mo and Nb and of Mo-Rich-Re, Mo-Nb, and Nb-Rich-Zr alloys. *Phys. Rev. B* **7**, 3580–3588 (1973).
33. Fu, Y. et al. $Mg_3(Bi,Sb)_2$-based thermoelectric modules for efficient and reliable waste-heat utilization up to 750 K. *Energy Environ. Sci.* **15**, 3265–3274 (2022).
34. Hu, Z., Fu, Y., Jiang, M., Wang, L. & Jiang, W. Thermal stability of Nb/Mg_3SbBi interface. *J. Inorg. Mater.* **38**, 931 (2023).
35. Li, J. et al. Bi-deficiency leading to high-performance in $Mg_3(Sb,Bi)_2$-based thermoelectric materials. *Adv. Mater.* **35**, 2209119 (2023).
36. Minnich, A. J., Dresselhaus, M. S., Ren, Z. F. & Chen, G. Bulk nanostructured thermoelectric materials: current research and future prospects. *Energy Environ. Sci.* **2**, 466 (2009).
37. Gayner, C. & Amouyal, Y. Energy filtering of charge carriers: current trends, challenges, and prospects for thermoelectric materials. *Adv. Funct. Mater.* **30**, 1901789 (2020).
38. Wang, L. et al. Realizing high thermoelectric performance in N-Type $Mg_3(Sb, Bi)_2$-based materials via synergetic Mo addition and Sb–Bi ratio refining. *Adv. Energy Mater.* **13**, 2301667 (2023).
39. Chen, X. et al. Excellent thermoelectric performance of boron-doped n-type Mg_3Sb_2-based materials via the manipulation of grain boundary scattering and control of Mg content. *Sci. China Mater.* **64**, 1761–1769 (2021).
40. Chen, X. et al. Extraordinary thermoelectric performance in n-type manganese doped Mg_3Sb_2 Zintl: high band degeneracy, tuned carrier scattering mechanism and hierarchical microstructure. *Nano Energy* **52**, 246–255 (2018).
41. Liang, J. et al. Synergistic effect of band and nanostructure engineering on the boosted thermoelectric performance of n-type $Mg_{3+\delta}(Sb, Bi)_2$ Zintls. *Adv. Energy Mater.* **12**, 2201086 (2022).
42. Zhu, B., Wang, W., Cui, J. & He, J. Point defect engineering: Co-doping synergy realizing superior performance in n-Type Bi_2Te_3 thermoelectric materials. *Small* **17**, 2101328 (2021).
43. Zhu, B. et al. Realizing record high performance in n-type Bi_2Te_3-based thermoelectric materials. *Energy Environ. Sci.* **13**, 2106–2114 (2020).

44. Kim, H.-S., Gibbs, Z. M., Tang, Y., Wang, H. & Snyder, G. J. Char-
    acterization of Lorenz number with Seebeck coefficient measure-
    ment. *APL Mater.* **3**, 041506 (2015).
45. Bu, Z. et al. An over 10% module efficiency obtained using non-
    Bi_2Te_3 thermoelectric materials for recovering heat of <600 K.
    Energy Environ. Sci. **14**, 6506–6513 (2021).
46. Yin, L. et al. Reliable N-type $Mg_{3.2}Sb_{1.5}Bi_{0.49}Te_{0.01}$/304 stainless
    steel junction for thermoelectric applications. *Acta Mater.* **198**,
    25–34 (2020).
47. Ying, P. et al. Towards tellurium-free thermoelectric modules for
    power generation from low-grade heat. *Nat. Commun.* **12**,
    1121 (2021).
48. Zhuang, H. et al. Thermoelectric performance enhancement in
    BiSbTe alloy by microstructure modulation via cyclic spark plasma
    sintering with liquid phase. *Adv. Funct. Mater.* **31**, 2009681 (2021).

Acknowledgements

Author contributions

J.-F.L., J.-W.L. and H.-L.Z. conceptualized this work. J.-W.L. performed the
synthesis and thermoelectric property measurements. H.H. performed
the EBSD measurement. Q.Z. carried out the STEM measurement. Z.H.
and W.L. contributed to the preparation and measurement of single-leg
devices. J.-W.L., B.S. and L.C. performed the structure characterizations.
J.-W.L., H.-L.Z., J.Y., H.L. and Y.J. helped the analysis of the thermoelectric
property data. J.-W.L., H.-L.Z., J.Y. and J.-F.L. wrote the manuscript. All
authors participated in the data analysis and the manuscript editing.

Competing interests

The authors declare no competing interests.

Additional information